Front. Earth Sci. 2022, 16(2): 523–539
https://doi.org/10.1007/s11707-021-0944-3

RESEARCH ARTICLE

3D reconstruction of coal pore network and its application in CO_2-ECBM process simulation at laboratory scale

Huihuang FANG (✉)[1,2,3], Hongjie XU (✉)[3,1,2], Shuxun SANG[4,5], Shiqi Liu[4,5], Shuailiang SONG[6], Huihu LIU[1,2]

1 State Key Laboratory of Mining Response and Disaster Prevention and Control in Deep Coal Mines, Anhui University of Science and Technology, Huainan 232001, China
2 School of Earth and Environment, Anhui University of Science and Technology, Huainan 232001, China
3 Institute of Energy, Hefei Comprehensive National Science Center, Hefei 230000, China
4 Jiangsu Key Laboratory of Coal-based Greenhouse Gas Control and Utilization, China University of Mining and Technology, Xuzhou 221008, China
5 Low Carbon Energy Institute, China University of Mining and Technology, Xuzhou 221008, China
6 Shandong Provincial Lunan Geo-engineering Exploration Institute, Jining 272100, China

Abstract Three-dimensional (3D) reconstruction of the equivalent pore network model (PNM) using X-ray computed tomography (CT) data are of significance for studying the CO_2-enhanced coalbed methane recovery (CO_2-ECBM). The docking among X-ray CT technology, MATLAB, with COMSOL software not only can realize the 3D reconstruction of PNM, but also the CO_2-ECBM process simulation. The results show that the Median filtering algorithm enabled the de-noising of the original 2D CT slices, the image segmentation of all slices was realized based on the selected threshold, and the PNM can be constructed based on the Maximum Sphere algorithm. The mathematical model of CO_2-ECBM process fully coupled the expanded Langmuir equation. At the same time for CO_2 injection, CH_4 pressure tends to decrease with the increase of CO_2 pressure, but its difference is not obvious. The CH_4 pressure in the slice center changed a lot, while at the edge it changed a little under different CO_2 pressures. The injected CO_2 was transported to matrix along the macro and micro-fractures with continuous flow. The injected CO_2 first replaced the adsorbed CH_4 by covering the inner surface of macro-pores and meso-pores to form the single molecular layer adsorption of CO_2. Then they migrated to micro-pores by Fick's diffusion, sliding flow, and surface diffusion. Furthermore, the CO_2 replaced CH_4 adsorbed by volumetric filling in micro-pores, and formed the multi-molecular layer adsorption of CO_2. The gas pressure and migration path between CO_2 and CH_4 are opposite. This study can provide a theoretical basis for studying digital rock physics technology and enrich the development of CO_2-ECBM technology.

Keywords CO_2-ECBM, 3D reconstruction, numerical simulation, X-ray CT, COMSOL, Qinshui Basin

1 Introduction

The CO_2-enhanced coalbed methane recovery (CO_2-ECBM) cannot only increase CH_4 production but also reduce CO_2 emissions (Fang et al., 2019a; Zheng et al., 2020). As a geological carrier for CO_2 injection, the pore system is the storage carrier of CO_2/CH_4, and the fracture system is the diffusion and seepage carrier of CO_2/CH_4 (Wang et al., 2018a, 2018b; Cheng et al., 2020; Wang et al., 2020a; Li et al., 2020a). Therefore, the three-dimensional (3D) reconstruction of coal pore and fracture can provide not only a framework for studying the seepage characteristic of fluid in porous media, but also theoretical support for the practical application of CO_2-ECBM technology.

As for pore and fracture, the characterization method can be summarized as follows. 1) Pore size distribution: low temperature CO_2/N_2 adsorption and mercury intrusion porosimetry (Connell et al., 2016; Li et al., 2017; Ni et al., 2020a; Nie et al., 2020). 2) Morphological observation: naked eye observation, optical microscope analysis, and scanning electron microscope analysis (Cai et al., 2018; Zhang et al., 2018; Li et al., 2020b). 3) 3D imaging: X-ray computed tomography (CT) and focused ion beam scanning electron microscopy (Fang et al., 2019b; Wang

Received May 18, 2021; accepted August 23, 2021

E-mails: huihuangfang@aust.edu.cn (Huihuang FANG), xiaonzm@163.com (Hongjie XU)

et al., 2020b). Through the comparison of the above experimental methods, it can be concluded that X-ray CT, as a non-destructive and high-resolution scanning technology (Fang et al., 2020; Zhu et al., 2020), is the most direct and accurate method to reconstruct the pore and fracture structure.

Previous studies have shown that the X-ray CT technology has been used for the 3D reconstruction of coal structure (Fan et al., 2020), and the finite element software has been used for the CO_2-ECBM process simulation (Fang et al., 2019c, 2019d), but few researchers have performed the CO_2-ECBM process simulation in finite element software with pore and fracture structure as the geological support. Therefore, based on the data extracted by X-ray CT technology and the application of MATLAB software, the interconnected pores and throats can be extracted from the equivalent pore and fracture network model (PNM), and the STL file output can be imported into the finite element software for the CO_2-ECBM process simulation, which is a new research hotspot focus in the CO_2-ECBM direction (Fig. 1).

In this study, first, based on the data obtained by X-ray CT and the application of MATLAB software, the geological carrier needed for numerical simulation can be extracted from PNM. Secondly, the STL file of the interconnected PNM extracted from the MATLAB software can be imported into the COMSOL software (available at COMSOL website) for grid partitioning and debugging. Then, the CO_2-ECBM process can be numerically simulated in the COMSOL software. Finally, the dynamic characteristics of the CO_2-ECBM process and the constraining effect of the pore and fracture structure on this process are discussed (Fig. 1). the significance and innovation of this study can be reflected as follows: 1) the mathematical model for simulating the CO_2-ECBM process at laboratory scale was deduced. 2) The pore network model was reconstructed and visualized in 3D. 3) The comprehensive application of X-ray CT technology, MATLAB, and COMSOL software for the CO_2-ECBM process simulation was established. 4) The dynamic characteristics of the CO_2-ECBM process and the confining effect of the pore and fracture structure on such a process were analyzed and visualized. This study can provide a theoretical basis for the study of digital rock physics technology and enrich the development of CO_2-ECBM technology.

2 Geological background and sampling point distribution

2.1 Geological background of the study area

The research area is located in the southern part of the Qinshui Basin, which is bounded by the Jinhuo Fault Zone to the east and adjacent to the Taihang Mountain Uplift, the Huoshan Uplift, and the Wutai Mountain Uplift to the west, south, and north direction, respectively (Figs. 2(a)–2(b); Cai et al., 2011; Wang et al., 2019). The stratigraphic distribution has the typical characteristics of a synclinal basin, the outcrop layer at the margin is old and the outcrop layer in the basin is new (Wang et al., 2021; Zhang et al., 2021). The coal-bearing strata are mainly Carboniferous-Permian, and the 3# coal seam of the Shanxi Formation and the 15# coal seam of the Taiyuan Formation are the main mining coal seams in the study area, and their transverse distribution is relatively stable (Fang et al., 2017; Huang et al., 2019; Ni et al., 2020b), which provides favorable conditions for the implementation of the CO_2-ECBM project.

2.2 Sampling point

In this study, coal samples collected from Bofang (BF) colliery in the Qinshui Basin were taken as the research object (Fig. 2(b); Liu et al., 2017; Fang et al., 2017), and the packing, transportation, storage and basic testing of samples comply with relevant international standards (Liu

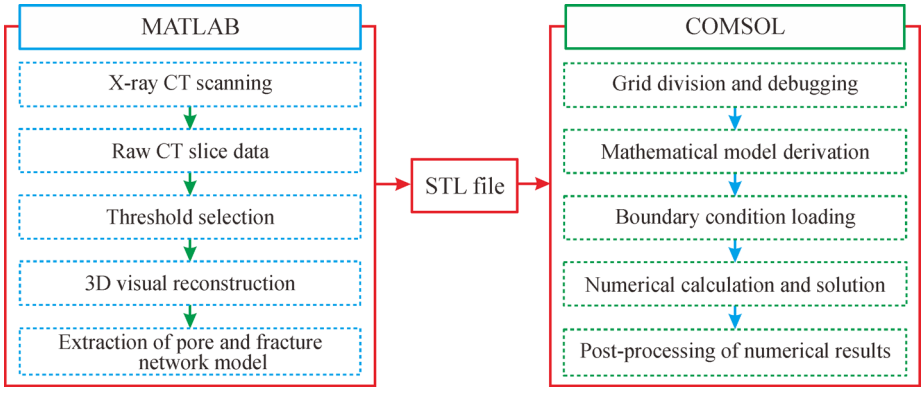

Fig. 1 General research idea of numerical simulation for CO_2-ECBM process based on the equivalent pore and fracture network model. (Note: File with the suffix STL plays a bridge between communication MATLAB and COMSOL software).

et al., 2017; Fang et al., 2019e). The anti-oxidation treatment of the fresh samples collected can prevent the fresh samples from being oxidized (Fig. 2(c)), which will affect the accuracy of the physicochemical properties of sample. After testing, the key parameters of the coal samples are shown in Table 1.

3 Methods

3.1 Reconstruction method of pore and fracture structure

3.1.1 X-ray CT scan imaging

In this study, the X-ray CT scanning imaging system is composed of the X-ray source, precision sample table, high-resolution detector, data processing system and controller system (Fig. 3). The sample used for scanning is a small coal column with a diameter of 2 mm and a height of about 6 mm, which was drilled with a prototype mechanical drill (Fig. 3(a)). The scanning area is a small coal column with a diameter of 2 mm and a height of 1 mm, the total number of scans is 3600, the pixel resolution is 0.5 μm, the spatial resolution is 200 nm, and the typical 2D CT slices are shown in Fig. 3(c). The gray, black and white areas within the perimeter can represent the distribution of organic matter, pores and minerals in coal, respectively (Fig. 3(c)).

3.1.2 3D reconstruction method of pore and fracture structure

To extract the geological carrier needed for the CO_2-ECBM process simulation, i.e., to extract the interconnected PNM in coal, the scanned 2D CT slices must be visually reconstructed, and the main tasks are as follows: preprocessing of the 2D slices, threshold selection and image segmentation, analysis of the representative elementary volume (REV), and construction of the pore network model.

Preprocessing of 2D slices: Due to uncontrollable factors, such as the X-ray CT scanner, the original CT slices extracted under noise lead to certain errors in the reconstruction of the coal structure at the later stage. Previous studies have shown that the noise reduction, such as the Median Filtering algorithm, for the original 2D slices can well protect the integrity of pores and smooth the transition between pore and matrix (Li and Zhang 2019; Fang et al., 2020), which provides a good basic for 3D reconstruction of coal structure.

Threshold selection and image segmentation: Converting 2D slices into a 3D image is the purpose of threshold segmentation, so that the pores can be separated from the matrix. The image segmentation method based on the selected threshold value is widely used in image segmentation. Its core idea is to determine the threshold value for image segmentation based on the gray histogram

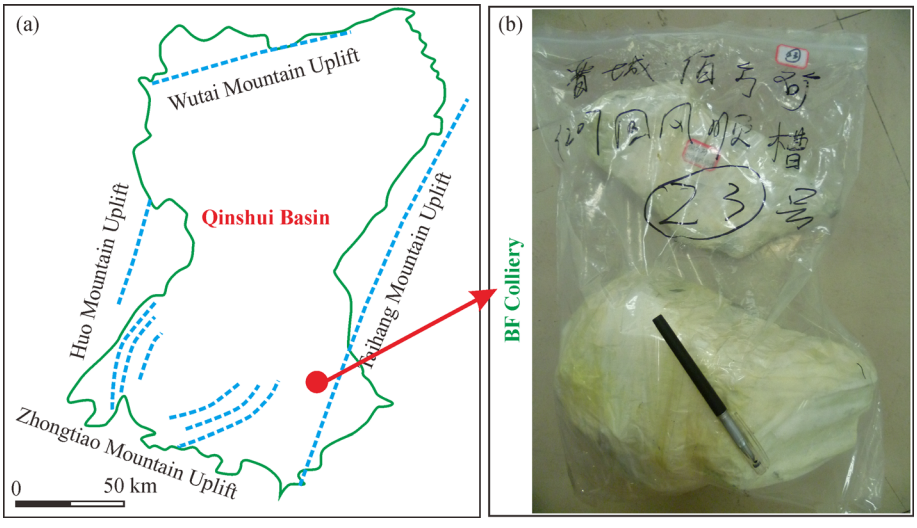

Fig. 2 Geological setting of the Qinshui Basin. (a) Four uplift belts in the Qinshui Basin (Modified from Cai et al., 2011), and (b) Anti-oxidation treatment of coal sample.

Table 1 Key properties of coal sample used in this study

Sampling location	$R_{o,max}$/%	Proximate analysis/(wt. %)				Ultimate analysis/(wt. %)			
		M_{ad}	A_{ad}	V_{daf}	FC_{ad}	O_{daf}	C_{daf}	H_{daf}	N_{daf}
BF	2.83	2.05	9.40	9.86	81.67	2.42	91.82	3.85	1.06

Notes: wt. %, weight percent; $R_{o,max/\%}$, average maximum vitrinite reflectance; M_{ad}, moisture; A_{ad}, ash yield; V_{daf}, volatile matter; FC_{ad}, fixed carbon content; O_{daf}, content of oxygen; C_{daf}, content of carbon; H_{daf}, content of hydrogen; N_{daf}, content of nitrogen; "ad", air-drying base; "daf", dry ash-free basis.

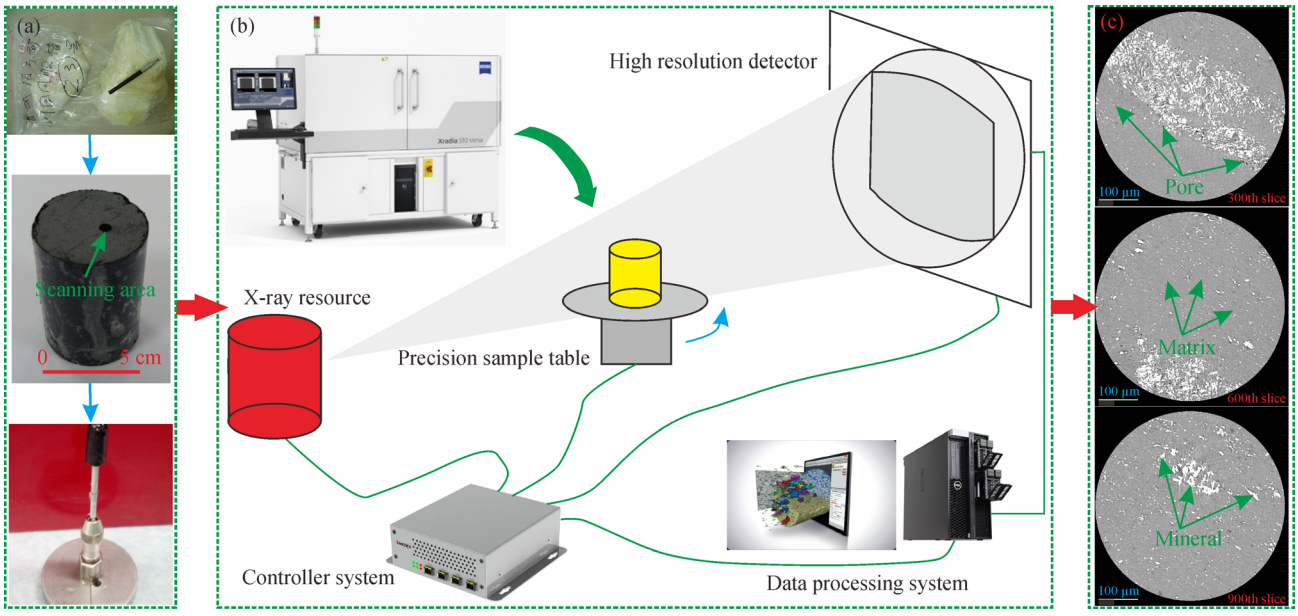

Fig. 3 X-ray CT scanning system. (a) Preparation of sample; (b) imaging system components; (c) typical 2D CT slices of BF coal sample.

of the image. In the current study, the gray histogram of the slices has single peak mode, while only a few samples have double peak mode. When the gray histogram of the image is bimodal, the local gray minimum can be used as the threshold for image segmentation.

Analysis of representative elementary volume: The representative elementary volume (REV) has the smallest size, but it contains all the information that can represent the physical property of the coal reservoir, and it is statistically significant (Vik et al., 2013; Yuan et al., 2016; Harpreet, 2017; Fang et al., 2020). The petrophysical property obtained with a size smaller than REV varies significantly, while the size larger than REV tends to be stable. By analyzing the law of variation of porosity and REV size, the size of REV can be determined.

Construction of pore network model: The Maximum Sphere algorithm is good at capturing the topological and geometrical structures of the pore and fracture, and is widely used to construct the PNM (Silin and Patzek, 2006; Lei et al., 2018). First, taking any point in the pore space as a basing point, the maximum inscribed sphere with this point as the circle center and tangent to the skeleton boundary is constantly searched. Secondly, when all the inscribed spheres are found, the other inscribed spheres contained in the inscribed spheres are removed, and the remaining inscribed spheres form the sphere set. Then, the clustering algorithm can be used to classify and summarize the maximum sphere and identify the pore and the throat. Finally, the pores can be represented as larger spheres and the throats as a set of smaller spheres (Fig. 4).

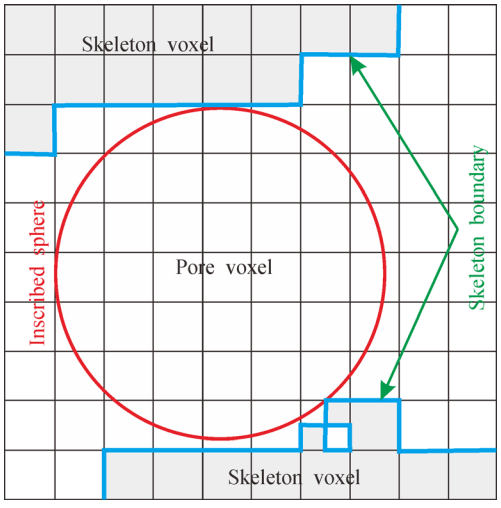

Fig. 4 Sketch of the Maximum Ball algorithm.

3.2 Numerical simulation method of CO_2-ECBM process

3.2.1 Mathematical model

To realize the numerical analysis of CO_2-ECBM process on laboratory scale, the mathematical model considering the parameter of pore and fracture structure should be established. In this study, the expanded Langmuir equation of competitive adsorption and the theoretical equation of adsorption, desorption and diffusion of CO_2 and CH_4 should be fully coupled in the mathematical model.

The gas diffusion in matrix is mainly controlled by its own concentration and follows Fick's law (Clarkson and Bustin, 1999; Sun et al., 2018). Based on Fick's first law, the continuity equation of gas adsorption and diffusion in matrix is shown in Eq. (1), namely Fick's second law with containing gas source term S (Fick, 1855; Sun et al., 2018):

$$\frac{\partial C}{\partial t}-D\nabla C=S, \tag{1}$$

where C is the gas concentration, mol/L, which is closely related to the spatial position (x, y, z) of gas and the time (t) analyzed; and D is the gas diffusion coefficient, m^2/s.

For fully coupled theoretical equations of gas adsorption and diffusion, the S in Eq. (1) can be characterized by the change of gas concentration adsorbed by the matrix over time:

$$S=-\frac{\partial C_{\mathrm{ad}}}{\partial t}, \tag{2}$$

where C_{ad} is the concentration of adsorbed gas in matrix, mol/L, which can be expressed as follows:

$$C_{\mathrm{ad}}=\frac{n_{\mathrm{ad}}}{V_{\mathrm{e}}}=\frac{sv/V_{\mathrm{m}}}{V_{\mathrm{e}}}=\frac{sv}{V_{\mathrm{m}}V_{\mathrm{e}}}, \tag{3}$$

where n_{ad} is the gas amount adsorbed by matrix, mol; V_{e} is the volume of grid elements, m^3; s is the pore surface area within the grid element, nm^2; v is the gas amount adsorbed within the pore surface area per unit, mL; and V_{m} is the gas molar volume, 22.4 L/mol.

The v in Eq. (3) can be calculated by the following equation (Sun et al., 2018):

$$v=\frac{VN_{\mathrm{solid}}V_{\mathrm{voxel}}\rho_{\mathrm{true}}}{f}, \tag{4}$$

where V is the gas volume adsorbed in coal per unit mass, m^3; f is the total pore surface area, m^2; N_{solid} is the total number of solid voxel; V_{voxel} is the volume per unit voxel, m^3; and ρ_{true} is the true coal density, kg/m^3.

For CO_2-ECBM process simulation on laboratory scale, it should be assumed that the gas is adsorbed only on the inner surface of the pore. When the gray value of voxel with $g(x, y, z)$ of the position (x, y, z) meets the following conditions (Eq. (5)), the inner surface of the pore can be marked:

$$\left\{\begin{array}{l} g(x,y,z)-g(x+1,y,z)=-1,\ \text{or} \\ g(x,y,z)-g(x,y+1,z)=-1,\ \text{or} \\ g(x,y,z)-g(x,y,z+1)=-1,\ \text{or} \\ g(x-1,y,z)-g(x,y,z)=-1,\ \text{or} \\ g(x,y-1,z)-g(x,y,z)=-1,\ \text{or} \\ g(x,y,z-1)-g(x,y,z)=-1 \end{array}\right\}, \tag{5}$$

where the gray value of pore voxels is 1, and the gray value of other voxels is 0.

For the bi-component gas of CH_4/CO_2, the C_{ad} in Eq. (2) can be characterized by the following extended Langmuir equation, and the diffusion theory of each component independently of other components has also been verified in the CO_2-ECBM pilot test (Shi and Durucan, 2005; Shi et al., 2008; Sun et al., 2018):

$$V_{\mathrm{CH_4}}=\frac{a_{\mathrm{CH_4}}b_{\mathrm{CH_4}}P_{\mathrm{CH_4}}}{1+b_{\mathrm{CH_4}}P_{\mathrm{CH_4}}+b_{\mathrm{CO_2}}P_{\mathrm{CO_2}}}, \tag{6}$$

$$V_{\mathrm{CO_2}}=\frac{a_{\mathrm{CO_2}}b_{\mathrm{CO_2}}P_{\mathrm{CO_2}}}{1+b_{\mathrm{CH_4}}P_{\mathrm{CH_4}}+b_{\mathrm{CO_2}}P_{\mathrm{CO_2}}}, \tag{7}$$

where $V_{\mathrm{CH_4}}$ and $V_{\mathrm{CO_2}}$ are the adsorption volume of CH_4 and CO_2, respectively, m^3/kg; $P_{\mathrm{CH_4}}$ and $P_{\mathrm{CO_2}}$ are gas pressure of CH_4 and CO_2, respectively, Pa; $a_{\mathrm{CH_4}}$ and $a_{\mathrm{CO_2}}$ are the Langmuir volume of CH_4 and CO_2, respectively, m^3/kg; and $b_{\mathrm{CH_4}}$ and $b_{\mathrm{CO_2}}$ are Langmuir pressure of CH_4 and CO_2, respectively, 1/Pa.

Considering the gas compressibility, the gas state equation can be characterized as follows:

$$C=\frac{n}{V}=\frac{P}{ZRT}=\frac{P}{f(T,P)RT}, \tag{8}$$

where Z is the compression factor, which is related to temperature and pressure; T is temperature, K; and P is pressure, MPa.

Based on the above analysis, the fully coupled mathematical model of CO_2-ECBM process on laboratory scale can be expressed as follows:

$$\frac{\partial P_{\mathrm{CH_4}}}{\partial t}-D_{\mathrm{CH_4}}\Delta P_{\mathrm{CH_4}}=-Z_{\mathrm{CH_4}}RT\frac{\partial}{\partial t}\left[\frac{N_{\mathrm{solid}}V_{\mathrm{voxel}}\rho_{\mathrm{true}}sa_{\mathrm{CH_4}}b_{\mathrm{CH_4}}P_{\mathrm{CH_4}}}{fV_{\mathrm{m}}V_{\mathrm{e}}(1+b_{\mathrm{CH_4}}P_{\mathrm{CH_4}}+b_{\mathrm{CO_2}}P_{\mathrm{CO_2}})}\right], \tag{9}$$

$$\frac{\partial P_{\mathrm{CO_2}}}{\partial t}-D_{\mathrm{CO_2}}\Delta P_{\mathrm{CO_2}}=-Z_{\mathrm{CO_2}}RT\frac{\partial}{\partial t}\left[\frac{N_{\mathrm{solid}}V_{\mathrm{voxel}}\rho_{\mathrm{true}}sa_{\mathrm{CO_2}}b_{\mathrm{CO_2}}P_{\mathrm{CO_2}}}{fV_{\mathrm{m}}V_{\mathrm{e}}(1+b_{\mathrm{CH_4}}P_{\mathrm{CH_4}}+b_{\mathrm{CO_2}}P_{\mathrm{CO_2}})}\right]. \tag{10}$$

3.2.2 Numerical schemes

For CO_2-ECBM process simulation on laboratory scale, the numerical schemes are shown in Table 2. Scheme 1 mainly represents the visual results of the CO_2-ECBM process, and scheme 2 mainly discusses the effect of the CO_2 pressure injected on the CO_2-ECBM process.

Table 2 Numerical simulation schemes of CO_2-ECBM process on the laboratory scale

Numerical schemes	Parameter setting	Program purpose
Scheme 1	Injection pressure of CO_2= 1.2 times CH_4 initial pressure	Visual result of CO_2-ECBM
Scheme 2	Injection pressure of CO_2= 1.2 times CH_4 initial pressure	Effect of CO_2 pressure injected on CO_2-ECBM
	Injection pressure of CO_2= 2.4 times CH_4 initial pressure	
	Injection pressure of CO_2= 3.6 times CH_4 initial pressure	
	Injection pressure of CO_2= 4.8 times CH_4 initial pressure	
	Injection pressure of CO_2= 6.0 times CH_4 initial pressure	

3.2.3 Loading of boundary conditions

On the laboratory scale, the loading of boundary conditions for this simulation is shown in Fig. 5. The pores in the reservoir are saturated with CH_4 (1×10^{-2} Pa), and the CO_2 pressure is set to 0 Pa under the initial conditions. During the CO_2-ECBM process, the CH_4 pressure outside the pores, i.e., on the outer surface of the cube, remains saturated condition at 1×10^{-2} Pa, and the CO_2 pressure is set according to the numerical schemes in Table 2 (Fig. 5).

3.2.4 Numerical parameters

The simulation parameters required for this CO_2-ECBM process simulation were all derived from correlation analysis experiment, and the gas attribute parameters required for this simulation were set according to the attribute parameters of CH_4 and CO_2 (Table 3).

3.2.5 Development of numerical software

The COMSOL, an advanced multiphysical field finite element software, has a wide simulation capability and strong post-processing capability to analyze and solve the fully coupled mathematical equations, but no corresponding processing interface can be added, and the data optimization capability of post-processing is low. The MATLAB software can be used to extract the geological model required for numerical simulation, i.e., the PNM, and the simulation results can be optimized in MATLAB software after COMSOL processing (Fig. 6). Therefore, the comprehensive application of COMSOL and MATLAB software is very necessary.

For CO_2-ECBM process simulation, the COMSOL software can create a graphical user interface (GUI) to realize the construction of COMSOL and MATLAB simulation system, and the GUI can form an independent software package based on typical calculation methods. First, the MATLAB script can be called in the GUI of the COMSOL software to build the geological model, and the grid partitioning and optimization of the geological model can be realized. Secondly, based on the MATLAB script, the geological model grid can be recognized in the GUI of COMSOL software. Then, based on the built-in PDE function of COMSOL software, parameters, variables and boundary conditions can be set in the GUI, and the numerical simulation can be successfully completed. Finally, the script function and language in MATLAB wrote by ourselves can be called to perform 3D visualization and data optimization after COMSOL processing (Fig. 6). Based on the MATLAB script, the interaction and sharing of data between COMSOL and MATLAB software can be realized.

4 Results

4.1 3D reconstruction of pore and fracture structure

The 3D reconstruction of pore and fracture structure for typical 2D CT slices can extract the geological carrier, i.e.,

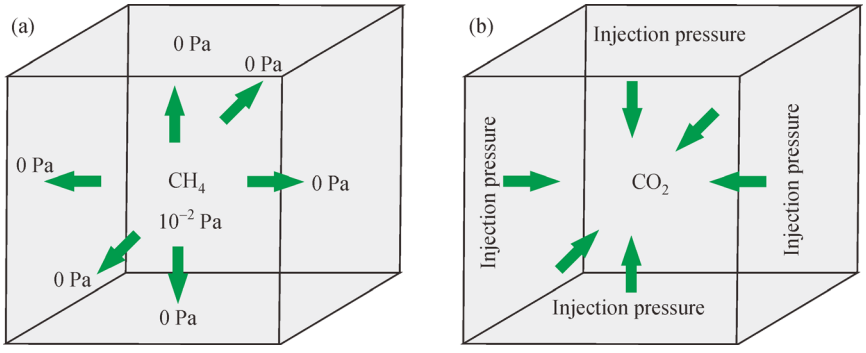

Fig. 5 Loading diagram of CH_4 and CO_2 boundary conditions during CO_2-ECBM process. (a) Initial conditions; (b) CO_2-ECBM process.

Table 3 Numerical simulation parameters of CO_2-ECBM process on the laboratory scale

Variables	Parameters	Value	Unit
R	Universal gas constant	8.314	J/(K·mol)
T	Simulation temperature	303	K
s	Pore surface area within the mesh element	5.4×10^{-9}	m^2
a_{CH_4}	Langmuir volume constant of CH_4	0.011	m^3/kg
b_{CH_4}	Langmuir pressure constant of CH_4	1.86×10^{-7}	1/Pa
a_{CO_2}	Langmuir volume constant of CO_2	0.0257	m^3/kg
b_{CO_2}	Langmuir pressure constant of CO_2	4.93×10^{-7}	1/Pa
V_m	Gas molar volume	0.0224	m^3/kg
f	Total pore surface area	1×10^{-9}	m^2
N_{solid}	Total number of solid voxels	2.2×10^{7}	—
V_{voxel}	Volume per unit voxel	1×10^{-18}	m^3
ρ_{true}	Coal density	1250	kg/m^3
V_e	Volume of grid element in numerical calculation	2.7×10^{-14}	m^3
D_1	Diffusion coefficient of CH_4	3.6×10^{-12}	m^2/s
D_2	Diffusion coefficient of CO_2	5.8×10^{-12}	m^2/s
P_{10}	Initial pressure of CH_4	1×10^{-2}	Pa

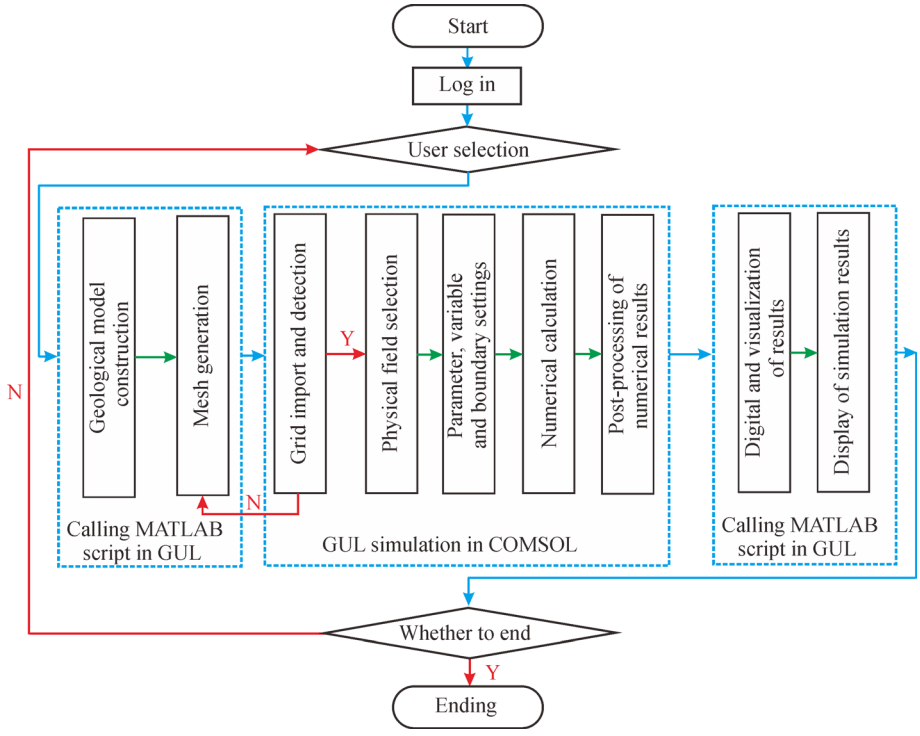

Fig. 6 Construction flow chart of the CO_2-ECBM simulation system based on the COMSOL and MATLAB software.

the PNM, needed for this numerical simulation. The preprocessing of 2D CT slices, threshold selection and image segmentation, analysis of REV, and construction of PNM are the key works, which are as follows:

4.1.1 Preprocessing of 2D CT slices

From Fig. 7(a), it can be seen that many noise points appeared in the original 2D CT slices. The Median

Filtering algorithm was used to process the 2D CT slices, and the results can be seen in Fig. 7(b). After filtering, the transition between skeleton and pore is smooth and natural, and the unrealistic outlier is no longer present in the image (Fig. 7). During the actual filtering, the filtered slices are often compared with the original slices to see whether some of the pores in coal have been erased.

4.1.2 Threshold selection and image segmentation

First, the frequency distribution histogram of gray can be calculated according to the gray distribution of the image. The gray range (H) is between 159 and 175 for BF sample (Fig. 8(b)). Second, a certain threshold (T_V) is selected based on the gray range (H) to divide the gray into two parts:$H_{0\to T_V}$, $H_{T_V+1\to 255}$, to calculate the variance $a(T_V)$ $=Var(H_{159\to T_V})$, $b(T_V)=Var(H_{T+1\to 175})$, and to calculate the difference of variance $D(T_V) = |a(T_V)\text{-}b(T_V)|$, where $T_V \in H$. Then, the threshold value T_V = find[max(D)] is defined to find the value of T_V in order to maximize D. Finally, after selecting T_V, the slice processed by T_V is often compared with the original 2D CT slice to detect whether some of the pores are deleted, and T_V can be partially fine-tuned (Fig. 8(b)). Based on this, the pores, organic matter and inorganic minerals of the BF sample can be extracted and reconstructed in 3D (Fig. 8(c)).

4.1.3 Extraction of pore network model

Analysis of the relationship between the porosity and the size of REV shows that when REV is larger than 500 × 500 × 500 voxel, porosity is relatively stable with the

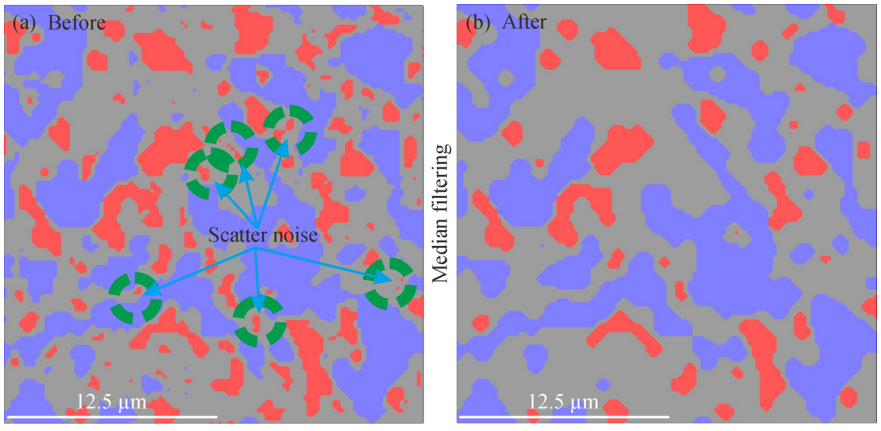

Fig. 7 Comparison of images before and after the Median Filtration. (a) Before Median Filtration; (b) after Median Filtration.

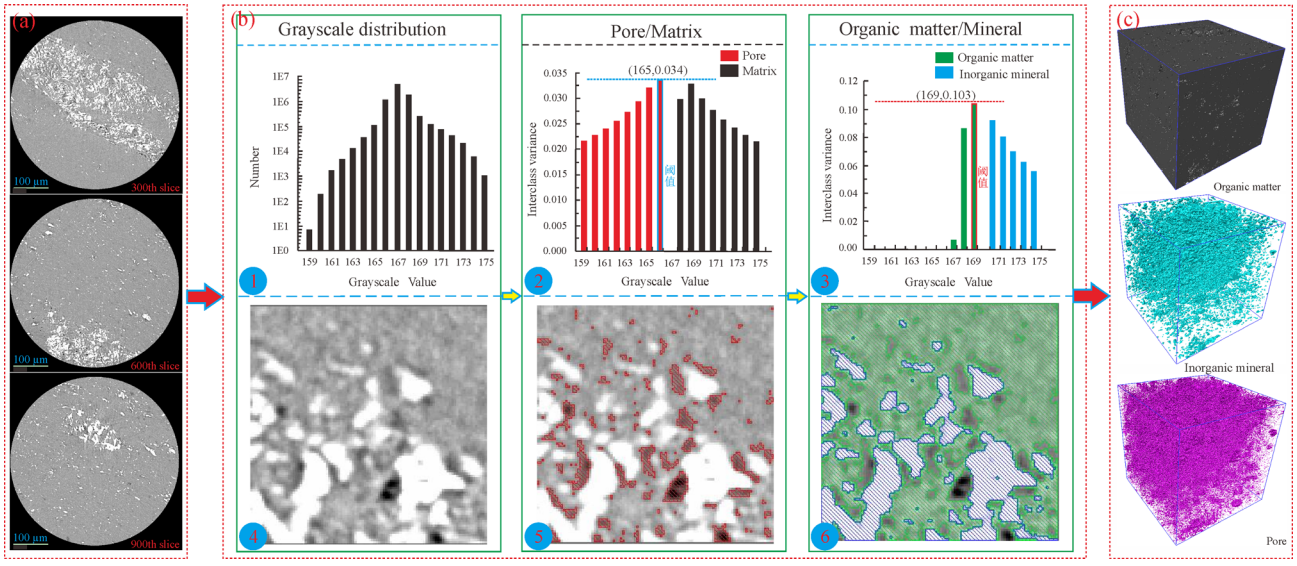

Fig. 8 Threshold selection and image segmentation. (a) Typical 2D CT slices; (b) threshold selection and image segmentation (1. greyscale distribution; 2. threshold selection of pore and matrix; 3. threshold selection of organic matter and inorganic mineral; 4. before segmentation; 5. segmentation of pore and matrix; 6. segmentation of organic matter and inorganic mineral); (c) 3D reconstruction of BF sample.

change of the REV size. Therefore, the 500 × 500 × 500 voxel can be selected to represent the size of REV (Fig. 9(a)). Based on the application of the Maximum Sphere algorithm (Fig. 9(b)), the pore and throat can be extracted from the PNM, separately (Fig. 9(c)).

4.2 Numerical result of the CO_2-ECBM process

4.2.1 Pre-treatment of the geological model

Based on the MATLAB software, the interconnected pores and throats can be extracted from the PNM, and the STL file can be imported into COMSOL software for the CO_2-ECBM process simulation, so as to bridge from the geometric model to the numerical simulation (Fig. 10). Given the computer memory capacity requirements of COMSOL software, when the sample size analyzed are larger than 60 × 60 × 60 voxel, the simulation process in COMSOL software will overflow due to the lack of computer memory. Therefore, a mesh size of 60 × 60 × 60 voxel was chosen for the CO_2-ECBM numerical analysis (Fig. 10(a)). Due to the complexity of pore and fracture

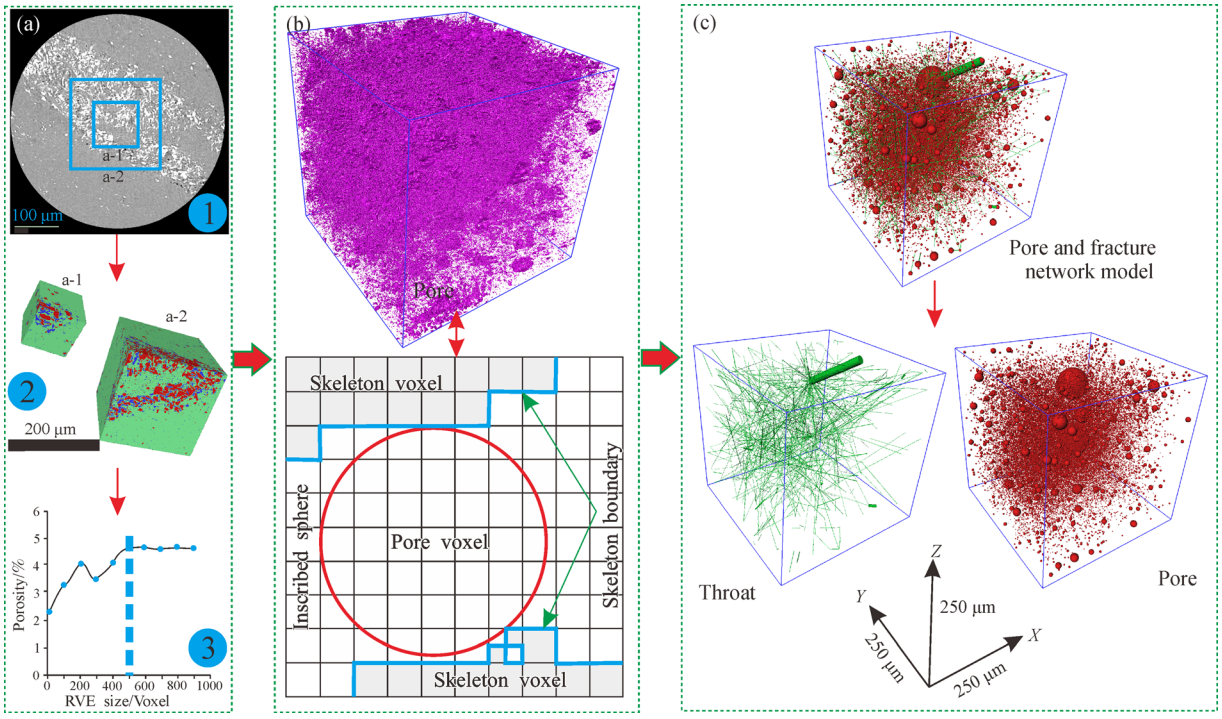

Fig. 9 Schematic diagram of REV analysis and extraction of pore and fracture network model. (a) REV analysis (1. original 2D CT slice; 2. REV size; 3. relationship between porosity and REV size); (b) Application of Maximum Ball Algorithm; (c) Extraction of pore and throat in pore and fracture network model.

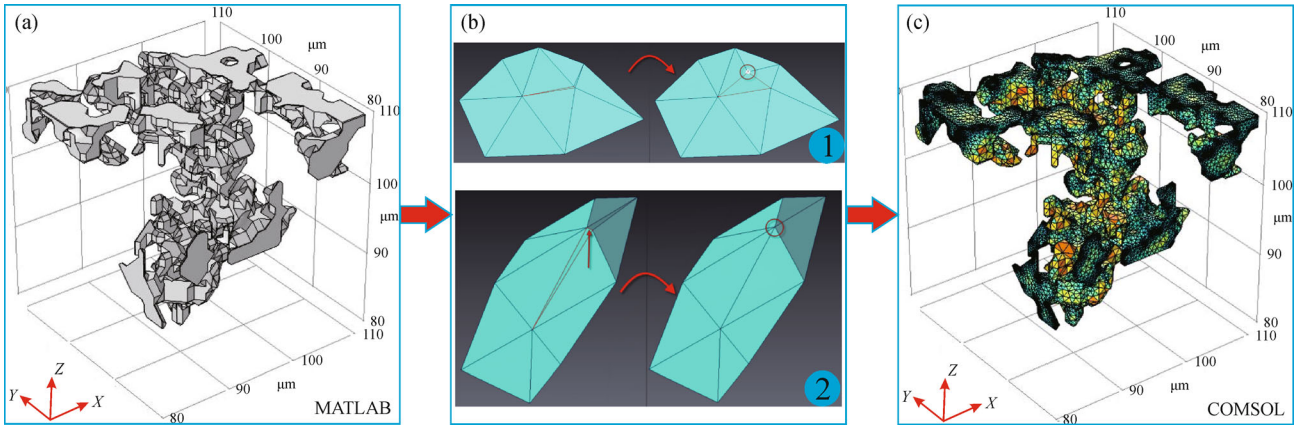

Fig. 10 P retreatment of geological model. (a) Interconnected pore and fracture network model; (b) surface detail repair of pore geometry model (1. editing a triangle with the Translate Vertex tool to improve model quality; 2. editing a triangle with the Contract Edges tool to improve model quality); (c) tetrahedral mesh without error.

structure, errors may occur in the meshing of geological model. Therefore, manual repair and debugging should be performed for the faulty geological model (Fig. 10(b)). Through continuous repair and debugging, the COMSOL software can generate the error-free tetrahedral mesh required for this numerical simulation (Fig. 10(c)).

4.2.2 Visualization of numerical results

Based on the COMSOL software, the post-processing and analysis of numerical results in laboratory scale were carried out, and the distribution of the pressure field of CO_2 and CH_4 in 3D, 2D and 1D can be obtained (Figs. 11–13).

Figure 11 shows the 3D distribution of CO_2 and CH_4 pressure during the CO_2-ECBM process. For CH_4, with the increase of CO_2 displacement time for CH_4, the CH_4 pressure gradually decreases at both the edge and the center of the simulation model (Fig. 11(a)). For CO_2, the CO_2 pressure gradually increases from the edge to the center of the simulation model with increasing CO_2 displacement time for CH_4 (Fig. 11(b)). During the whole period of CO_2 displacement for CH_4, the pressure drop was the same ($\Delta P = 0.01$ Pa), but the 3D distribution of gas pressure at different times and positions was greatly different (Fig. 11), which lies in the differences of radius, shape and connectivity of pore and throat. When CH_4 is displaced by CO_2, the area where CH_4 pressure gradually decreases are also the area where CO_2 pressure gradually increases (Fig. 11).

The pressure field in different slices was quantitatively analyzed. The CO_2 gradually disinfects the center from the edge of the model. Therefore, analysis should be performed with the positions of 85 μm (5th slice), 90 μm (10th slice), 95 μm (15th slice), 100 μm (20th slice), 105 μm (25th slice), and 110 μm (30th slice) and with the analysis time of 15th second, 30th second, 45th second and 60th second, respectively (Fig. 12). In the original 2D CT slices, the black area represents the matrix and the white area represents the pore and fracture, which are the geological carrier for CO_2-ECBM process simulation.

Figure 12 shows the 2D distribution of CO_2 and CH_4 pressure during the CO_2-ECBM process. For CH_4, as the time of CO_2 displacement increases, the gas pressure decreases from the center to the edge in all slices, and the total CH_4 pressure in reservoir also gradually decreases with time. At the same time, the CH_4 pressure in the central slices, such as the 10th, 15th, 20th and 25th slice, was relatively high, while that in the edge slices, such as the 5th and 30th slice, was relatively low (Fig. 12). For CO_2, the pressure distribution is opposite to that of CH_4. As the time of CO_2 displacement CH_4 increase, the CO_2 pressure increases from the edge to the center in all slices, and the total CO_2 pressure in reservoir also gradually increases with time. At the same time, the CO_2 pressure in the central slices, such as the 10th, 15th, 20th and 25th slice, was relatively low, while that in the edge slices, such as the 5th and 30th slice, was relatively high (Fig. 12).

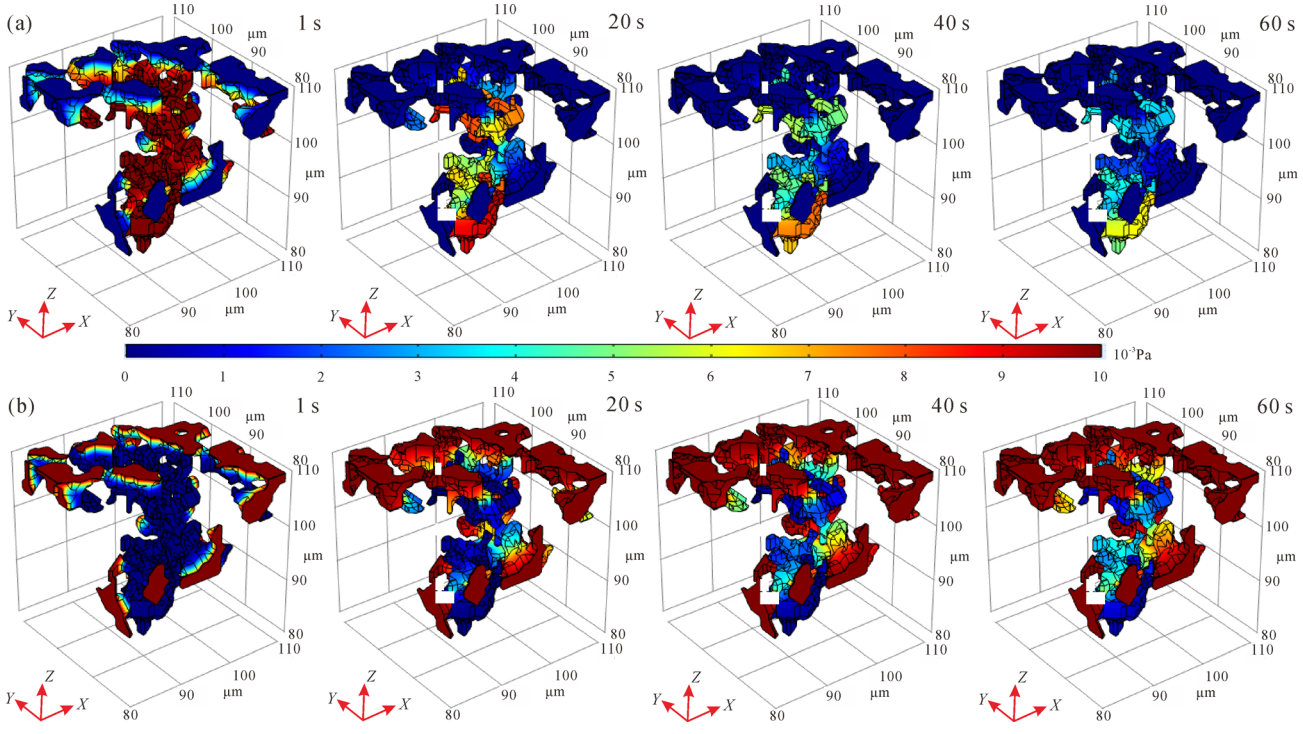

Fig. 11 3D distribution of gas pressure field during the CO_2-ECBM process. (a) CH_4; (b) CO_2.

In this study, three monitoring points of A(82, 128, 109), B(87, 120, 107) and C(96, 115, 104) were selected to quantitatively investigate the distribution law of CH_4 and CO_2 pressure at different positions over time (Fig. 13), and points A to C represent the position from the edge of the reservoir to the center.

Figure 13 shows the 1D distribution of CO_2 and CH_4 pressure during the CO_2-ECBM process. For CH_4, the CH_4 pressure at different positions gradually decreases with increasing CO_2 displacement time of CH_4. Here, the closer to the center of the model, the higher the CH_4 pressure, and the closer to the edge, the lower the CH_4 pressure (Fig. 13(a)). In terms of CO_2, the CO_2 pressure at different positions gradually increases with the increase of CO_2 displacement CH_4 time. Here, the closer it is to the center of the model, the lower the CO_2 pressure is, while the closer it is to the edge of the model, the higher the CO_2 pressure is (Fig. 13(b)). The gas pressure changes rapidly in the early stage (0−20 s) of CO_2 displacement CH_4 and slowly in the later stage (>20 s) (Fig. 13).

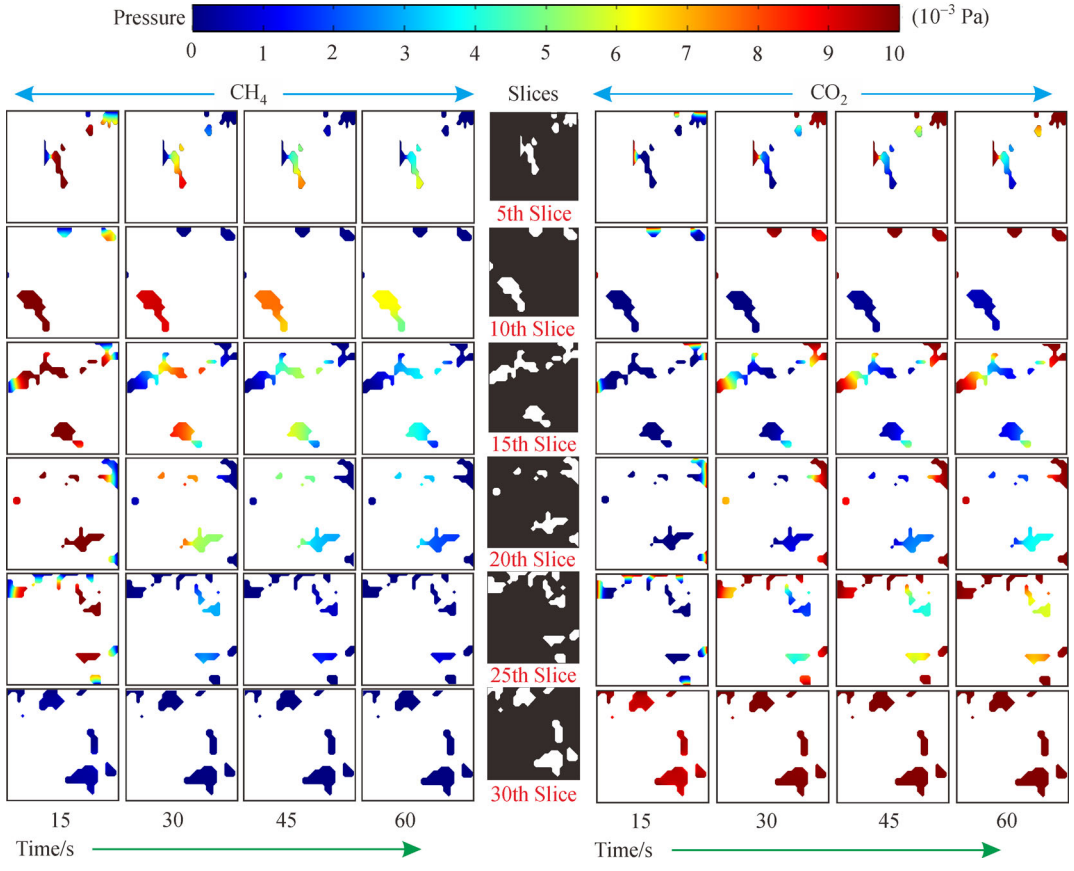

Fig. 12 2D distribution of gas pressure field during the CO_2-ECBM process.

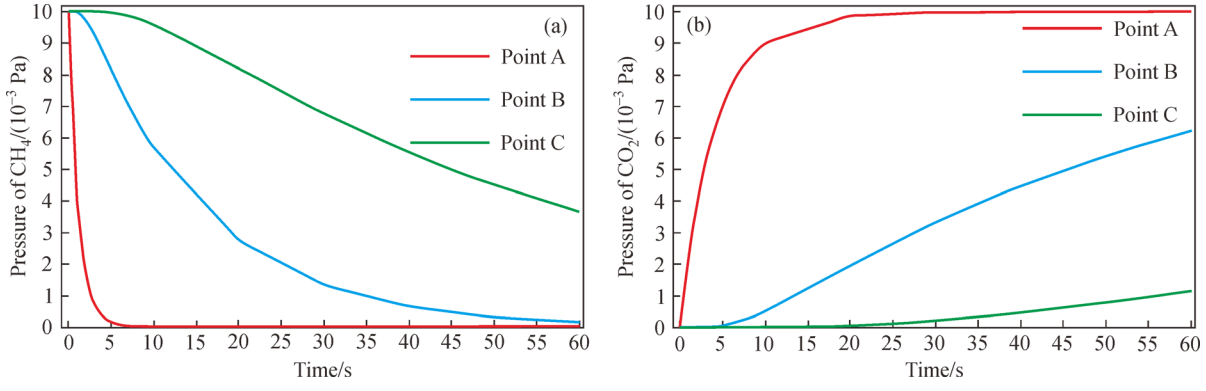

Fig. 13 Relationship curves of gas pressure and time at different position during the CO_2-ECBM process. (a) CO_2 pressure and time curves; (b) CH_4 pressure and time curves.

4.2.3 Effect of CO_2 pressure injected on the CO_2-ECBM process

The saturation pressure of CH_4 was kept at 1×10^{-2} Pa, and the effect of gas pressure injected on CO_2-ECBM process was analyzed by changing the CO_2 pressure injected according to the scheme 2. This part focuses on the analysis of the distribution law of CO_2.

Figure 14 shows the 3D distribution of the CO_2 pressure field when the CO_2 pressure injected is changed during the CO_2-ECBM process. At the same CO_2 injection time, the CO_2 pressure shows a trend of gradual increase with the increase of CO_2 pressure injected, and the differences of CO_2 pressure in reservoir are relatively clear at each CO_2 pressure injected. At different CO_2 pressures injected, the CO_2 pressure changes in reservoir are all large, and the CO_2 pressure changes in the center of the slice are relatively small, while those at the edge of the slice are relatively large (Fig. 14).

To further analyze the distribution of CO_2 pressure field in different slices under different pressures injected, the position of 95 μm on the *X*-axis was taken as an example for analysis, and the analysis time was 1st second, 10th second, 20th second, 40th second and 60th second (Fig. 15).

Figure 15 shows the 2D distribution of the CO_2 pressure field when the CO_2 pressure injected is changed during the CO_2-ECBM process. At the same gas injection time, the CO_2 pressure shows a trend of gradual increase with the increase of CO_2 pressure injected. For the same gas pressure injected, the CO_2 pressure gradually increases from the slice edge to the center as the increase of CO_2 injection time (Fig. 15).

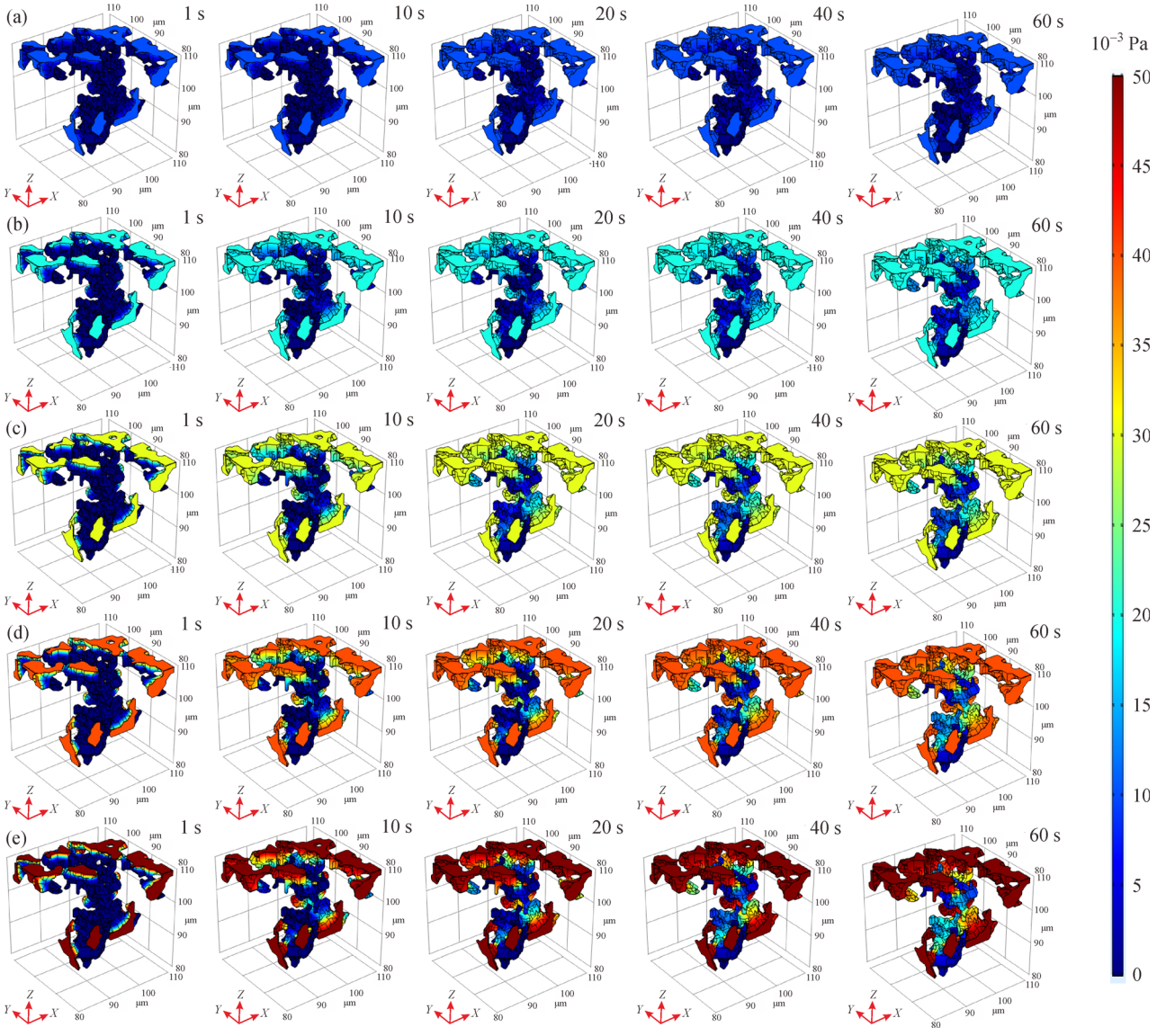

Fig. 14 Effect of CO_2 pressure injected on CO_2 pressure field during the CO_2-ECBM process. (a) 1.2 times CO_2 pressure injected; (b) 2.4 times CO_2 pressure injected; (c) 3.6 times CO_2 pressure injected; (d) 4.8 times CO_2 pressure injected; (e) 6.0 times CO_2 pressure injected.

Monitoring point B(87, 120, 107) was selected to quantitatively investigate the gas pressure changes in reservoir under different CO_2 pressures injected in the CO_2-ECBM process (Fig. 16).

Figure 16 shows the distribution of CO_2 pressure at point B at different CO_2 pressures injected. At different CO_2 pressures injected, the CO_2 pressure in pore gradually increases with increasing CO_2 injection time. At the same time, the higher the gas pressure injected, the faster the increasing rate of CO_2 pressure, which indicates that the diffusion and adsorption rates of CO_2 increase with the increase of gas pressure injected (Fig. 16). The higher the CO_2 pressure, the sooner the CO_2 pressure in pore reaches the steady-state, i.e., $T_{S5} > T_{S4} > T_{S3} > T_{S2} > T_{S1}$ (Fig. 16).

5 Discussion

5.1 Dynamic characteristics of the CO_2-ECBM continuous process

Figure 17 is a simple diagram of the continuous CO_2-ECBM process. Based on this figure and the previous discussion on CO_2-ECBM theory, the continuous process with adsorption, desorption, diffusion and percolation of CH_4 and CO_2 during the CO_2-ECBM process can be analyzed.

As for the CO_2, the CO_2 injected mainly migrates along the macro- and micro-fractures with continuous flow into the matrix. The CO_2 injected first replaces the CH_4 adsorbed by covering the inner surface of the macro- and the meso-pores, so that a single molecular layer of CO_2 is adsorbed. Then it migrates to the micro-pores by Fick's diffusion, slip flow and surface diffusion. Moreover, CO_2 replaces CH_4 adsorbed by volumetric filling of the micro-pores and forms a multi-molecular layer adsorption of CO_2 (Fig. 17). In the case of CH_4, the CH_4 in reservoir is saturated in the initial state, and CH_4 molecules maintain a dynamic equilibrium state of adsorption and desorption behavior in matrix. The injection of CO_2 disrupts this equilibrium of CH_4 in matrix. Since the matrix has a higher adsorption capacity for CO_2 than for CH_4, the matrix has priority in adsorption of CO_2 over desorption of CH_4 in the competition between CO_2 and CH_4, which can complete the process of CO_2 replacement of CH_4 (Fig. 17).

The CH_4 and CO_2 adsorbed on the inner surface of the

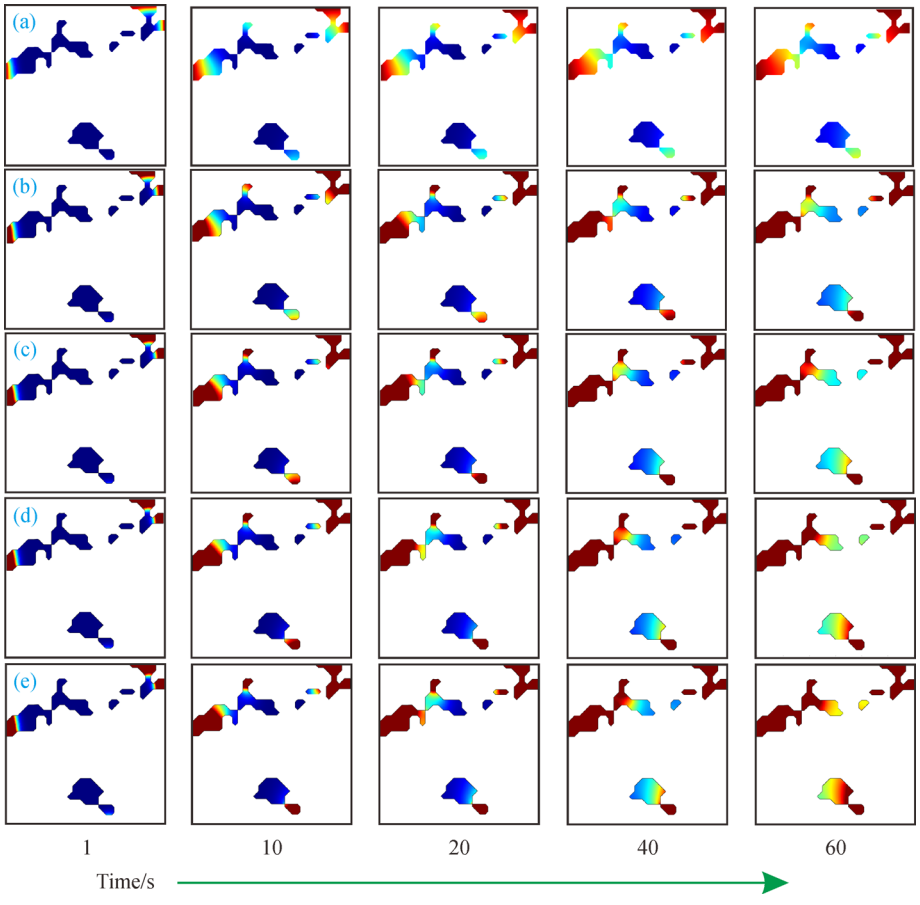

Fig. 15 2D distribution of CO_2 pressure under different CO_2 pressures injected during the CO_2-ECBM process (the 15th slice). (a) 1.2 times CO_2 pressure injected; (b) 2.4 times CO_2 pressure injected; (c) 3.6 times CO_2 pressure injected; (d) 4.8 times CO_2 pressure injected; (e) 6.0 times CO_2 pressure injected.

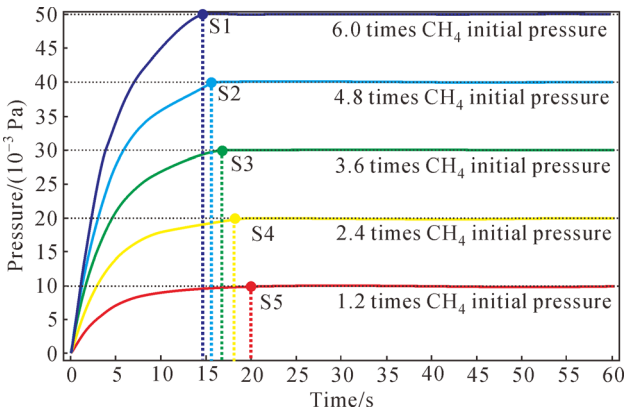

Fig. 16 CO_2 pressure distribution of point B under different CO_2 pressure injected during the CO_2-ECBM process.

matrix complete in the adsorption position. In general, the adsorption capacity of matrix is twice as high for CO_2 as for CH_4 (Fig. 18). The CH_4 desorbed diffuses from the surface of matrix into the micro-pores under the action of the concentration gradient, and the process follows Fick's law. Then, it moves from the pore to the fracture and then to the wellbore through seepage under the action of the pressure gradient, which follows Darcy's Law (Fig. 19). Based on the analysis of Dalton's law, in the CO_2-ECBM process, although the total gas pressure in reservoir remains unchanged, the partial pressure of CO_2 in reservoir increases with time, while the partial pressure of CH_4 decreases with time. The CO_2 injected in reservoir gradually replaces the CH_4 in reservoir through competitive adsorption, which improves the CH_4 recovery while storing CO_2 (Fig. 19).

5.2 Influential effect of pore and fracture structure on continuous CO_2-ECBM process

The coal reservoir can be abstracted as a dual-pore medium consisting of pores and fractures. The term "Double-Pore" refers to the pore system and the fracture system (Fig. 20). Pores are mainly evolved by physical and chemical processes during coal formation. Fractures are mainly formed by the late stress effect. In reservoir, the multilevel pore and fracture structure network formed by interconnected pores and fractures will affect the adsorption, desorption, diffusion and seepage of fluid in reservoir. The fluid is in dynamic equilibrium in reservoir, the pore system in matrix is mainly the adsorption space of fluid, and the migration channel of the fluid is mainly the fracture system.

The pore and fracture systems in reservoir form the multilevel network structure, and this is the main occurrence space and migration channel of CH_4 and CO_2 in the CO_2-ECBM process. The influential effect on the continuous process during the CO_2-ECBM process can be summarized as follows: (1) micro-pores and meso-pores in reservoir are the main occurrence place of CH_4 and CO_2 during the CO_2-ECBM process. (2) The migration and production path of CH_4 is from micro-pores, meso-pores, macro-pores, micro-fractures, endogenous fractures,

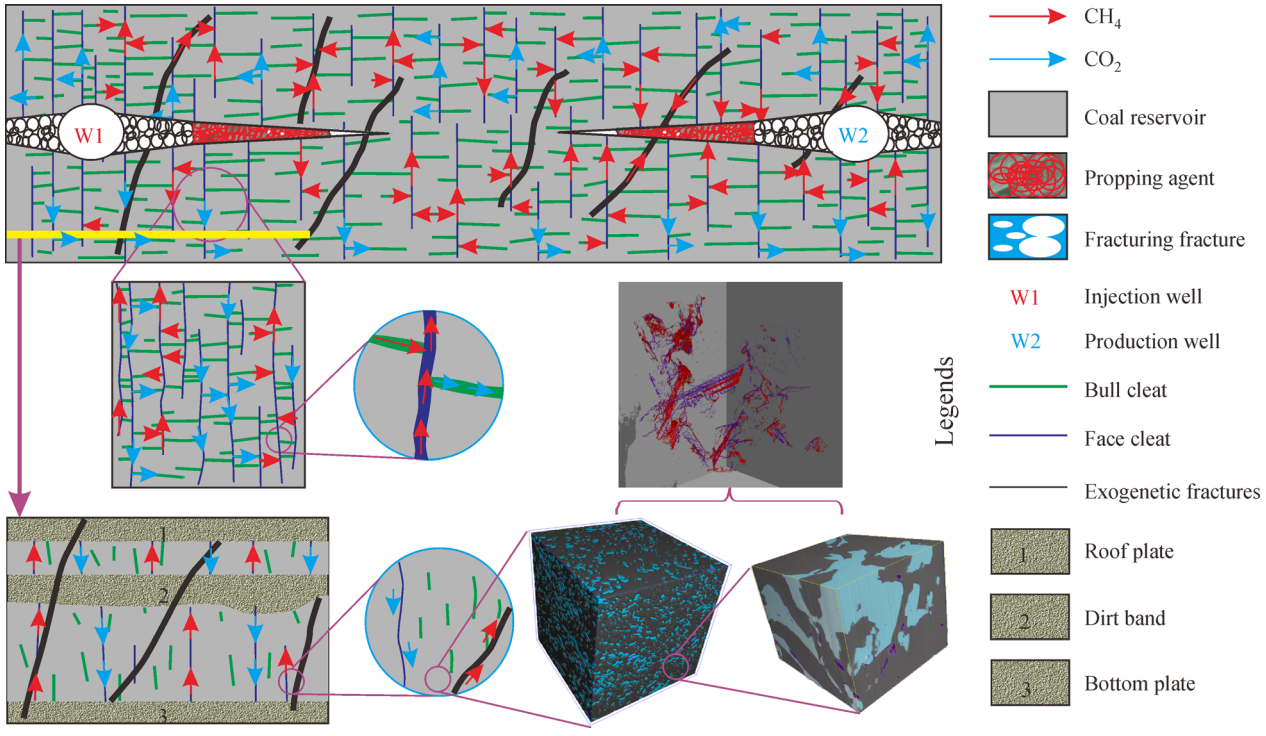

Fig. 17 Schematic diagram of CO_2-ECBM continuity process.

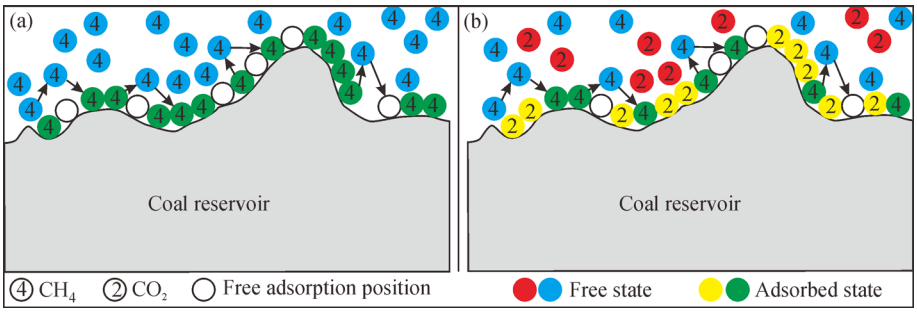

Fig. 18 Schematic diagram of CH_4 and CO_2 occupying adsorption sites. (a) Initial state of CH_4 in reservoir; (b) after CO_2 injection.

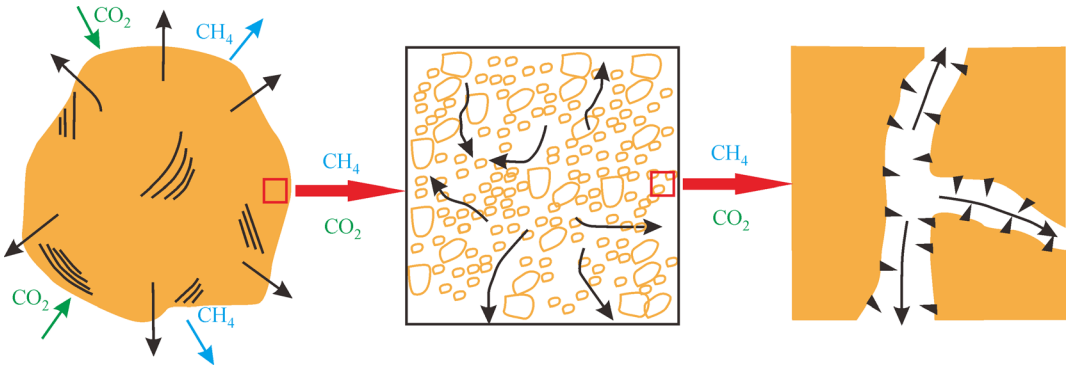

Fig. 19 Fluid dynamic characteristics of the CO_2-ECBM process (Modified from CERVIK, 1967).

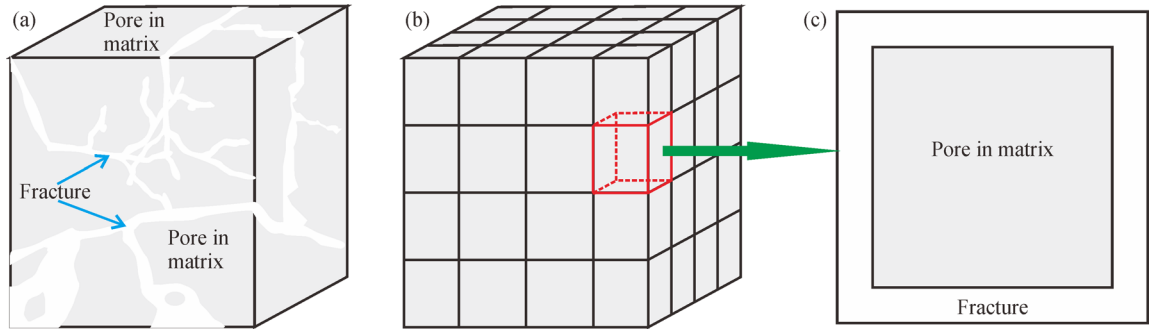

Fig. 20 Abstract schematic diagram of the Double Pore media of the coal reservoir (Wang et al., 2018a, 2018b). (a) Actual coal reservoir; (b) abstract coal reservoir; (c) schematic diagram of pore and fracture.

macro-fractures, to fracturing fractures during CO_2-ECBM process. (3) The migration path of CO_2 is exactly opposite to that of CH_4 during CO_2-ECBM process. (4) The output of CH_4 passes through three flow levels, i.e., from pores, natural fractures, fracturing fractures, to wellbore. (5) At the macro level, CO_2 injection also passes through three flow levels, which is from wellbores, fracturing fractures, natural fractures, to pores.

6 Conclusions

1) The perfect coupling among the X-ray CT technology, the MATLAB, with the COMSOL software cannot only realize the 3D reconstruction of pore network model, but also complete the CO_2-ECBM process simulation, and further investigate the influential effect of PNM on such process. The Median filtering algorithm enables the de-noising of the original 2D CT slices, the threshold selection and image segmentation are realized based on the image segmentation method, and the PNM can be constructed based on the Maximum Sphere algorithm.

2) The CO_2-ECBM mathematical model considering PNM parameter completely couples the expanded Langmuir equation of competitive adsorption and the theoretical equation of adsorption, desorption and diffusion of CO_2/

CH_4. At the same injection time, CH_4 pressure gradually decrease with the increase of CO_2 pressure injected, but the difference of CH_4 pressure at each CO_2 pressure is not obvious. At different CO_2 pressures, the CH_4 pressure changed a lot at the slice center, while it changed a little at the slice edge. The law of change of CO_2 pressure is opposite to that of CH_4 pressure.

3) The CO_2 injected is transported into the matrix along the macro- and micro-fractures with continuous flow. The CO_2 injected first replaces the CH_4 adsorbed by covering the inner surface of the macro-pores and the meso-pores to form the adsorption of CO_2 in a single molecular layer. Then they migrate to the micro-pores by Fick's diffusion, slip flow and surface diffusion. Moreover, the CO_2 replaces the CH_4 adsorbed in the micro-pores by volumetric filling and forms the multi-molecular layer adsorption of CO_2. The migration path of CH_4 is opposite to that of CO_2.

Acknowledgements We would like to express our gratitude to the anonymous reviewers for offering their constructive suggestions and comments which improved this manuscript in many aspects. This work was financially supported by the Institute of Energy, Hefei Comprehensive National Science Center (No. 21KZS218), the University Synergy Innovation Program of Anhui Province (No. GXXT-2021-018), the Natural Science Research Project of Anhui University (Nos. KJ2020A0315, KJ2020A0317), the Natural Science Foundation of Anhui Province (No. 2108085MD134), the National Natural Science Foundation of China (No. 41902168), and the Foundation of State Key Laboratory of Petroleum Resources and Prospecting, China University of Petroleum, Beijing (No. PRP/open-2005).

References

Cai Y D, Liu D M, Yao Y B, Li J G, Qiu Y K (2011). Geological controls on prediction of coalbed methane of No. 3 coal seam in Southern Qinshui Basin, North China. Int J Coal Geol, 88(2–3): 101–112

Cai T T, Feng Z C, Zhou D (2018). Multi-scale characteristics of coal structure by X-ray computed tomography (X-ray CT), scanning electron microscope (SEM) and mercury intrusion porosimetry (MIP). AIP Adv, 8(2): 025324

Cervik J (1967). Behavior of coal-gas reservoirs. In: SPE Eastern Regional Meeting

Cheng G X, Jiang B, Li M, Li F L, Song Y (2020). Effects of pore-fracture structure of ductile tectonically deformed coals on their permeability: an experimental study based on raw coal cores. J Petrol Sci Eng, 193: 107371

Clarkson C R, Bustin R M (1999). The effect of pore structure and gas pressure upon the transport properties of coal: a laboratory and modeling study. Fuel, 78(11): 1345–1362

Connell L D, Mazumder S, Sander R, Camilleri M, Pan Z J, Heryanto D (2016). Laboratory characterization of coal matrix shrinkage, cleat compressibility and the geo-mechanical properties determining reservoir permeability. Fuel, 165: 499–512

Fan N, Wang J R, Deng C B, Fan Y P, Wang T T, Guo X Y (2020). Quantitative characterization of coal microstructure and visualization seepage of macropores using CT-based 3D reconstruction. J Nat Gas Sci Eng, 81: 103384

Fang H H, Sang S X, Wang J L, Liu S Q, Ju W (2017). Simulation of paleotectonic stress fields and distribution prediction of tectonic fractures at the Hudi Coal Mine, Qinshui Basin. Acta Geol Sin-Engl, 91(6): 2007–2023

Fang H H, Sang S X, Liu S Q (2019a). Establishment of dynamic permeability model of coal reservoir and its numerical simulation during the CO_2-ECBM process. J Petrol Sci Eng, 179: 885–898

Fang H H, Sang S X, Liu S Q, Du Y (2019b). Methodology of three-dimensional visualization and quantitative characterization of nanopores in coal by using FIB-SEM and its application with anthracite in Qinshui Basin. J Petrol Sci Eng, 182: 106285

Fang H H, Sang S X, Liu S Q (2019c). The coupling mechanism of the thermal-hydraulic-mechanical fields in CH_4-bearing coal and its application in the CO_2-enhanced coalbed methane recovery. J Petrol Sci Eng, 181: 106177

Fang H H, Sang S X, Liu S Q (2019d). Numerical simulation of enhancing coalbed methane recovery by injecting CO_2 with heat injection. Petrol Sci, 16(1): 32–43

Fang H H, Sang S X, Liu S Q, Liu S P (2019e). Experimental simulation of replacing and displacing CH_4 by injecting supercritical CO_2 and its geological significance. Int J Greenh Gas Control, 81: 115–125

Fang H H, Sang S X, Liu S Q (2020). Three-dimensional spatial structure of the macro-pores and flow simulation in anthracite coal based on X-ray mu-CT scanning data. Petrol Sci, 17(5): 1221–1236

Fick A (1855). On liquid diffusion. Philos Mag, 10(63): 30–39

Huang S P, Liu D M, Cai Y D, Gan Q (2019). *In situ* stress distribution and its impact on CBM reservoir properties in the Zhengzhuang area, southern Qinshui Basin, North China. J Nat Gas Sci Eng, 61: 83–96

Lei J, Pan B Z, Zhang L H (2018). Advance of microscopic flow simulation based on digital cores and pore network. Prog Geophys, 33(2): 653–660 (in Chinese)

Li Y, Zhang C, Tang D, Gan Q, Niu X, Wang K, Shen R (2017). Coal pore size distributions controlled by the coalification process: an experimental study of coals from the Junggar, Ordos, and Qinshui basins in China. Fuel, 206: 352–363

Li Z W, Zhang G Y (2019). Fracture segmentation method based on contour evolution and gradient direction consistency in sequence of coal rock CT images. Math Probl Eng, 1: 1–82980747

Li Y, Wang Y, Wang J, Pan Z (2020a). Variation in permeability during CO_2-CH_4 displacement in coal seams: part I-Experimental insights. Fuel, 263: 116666

Li Y, Yang J, Pan Z, Tong W (2020b). Nanoscale pore structure and mechanical property analysis of coal: an insight combining AFM and SEM images. Fuel, 260: 116352

Liu S Q, Sang S X, Wang G, Ma J S, Wang T, Wang W, Du Y, Wang T (2017). FIB-SEM and X-ray CT characterization of interconnected pores in high-rank coal formed from regional metamorphism. J Petrol Sci Eng, 148: 21–31

Ni G H, Li S, Rahman S, Xun M, Wang H, Xu Y H, Xie H C (2020a). Effect of nitric acid on the pore structure and fractal characteristics of coal based on the low-temperature nitrogen adsorption method. Powder Technol, 367: 506–516

Ni X M, Zhao Z, Wang Y B, Wang L (2020b). Optimisation and application of well types for ground development of coalbed methane from No. 3 coal seam in shizhuang south block in Qinshui Basin, Shanxi Province, China. J Petrol Sci Eng, 193: 107453

Nie B S, Lun J Y, Wang K D, Shen J S (2020). Three-dimensional characterization of open and closed coal nanopores based on a multi-scale analysis including CO_2 adsorption, mercury intrusion, low-temperature nitrogen adsorption, and small-angle X-ray scattering. Energy Sci Eng, 8(6): 2086–2099

Shi J Q, Durucan S (2005). A model for changes in coalbed permeability during primary and enhanced methane recovery. SPE Reservoir Eval Eng, 8(04): 291–299

Shi J Q, Mazumder S, Wolf K H, Durucan S (2008). Competitive methane desorption by supercritical CO_2 injection in coal. Transp Porous Media, 75(1): 35–54

Silin D, Patzek T (2006). Pore space morphology analysis using maximal inscribed spheres. Physica A, 371(2): 336–360

Singh H (2017). Representative Elementary Volume (REV) in spatio-temporal domain: a method to find REV for dynamic pores. J Earth Sci, 28(2): 391–403

Sun Y F, Zhao Y X, Yuan L (2018). CO_2-ECBM in coal nanostructure: modelling and simulation. J Nat Gas Sci Eng, 54: 202–215

Vik B, Bastesen E, Skauge A (2013). Evaluation of representative elementary volume for a vuggy carbonate rock-Part: porosity, permeability, and dispersivity. J Petrol Sci Eng, 112(3): 36–47

Wang G, Wang K, Jiang Y J, Wang S Q (2018a). Reservoir permeability evolution during the process of CO_2-enhanced coalbed methane recovery. Energies, 11(11): 2996

Wang G, Wang K, Wang S G, Elsworth D, Jiang Y J (2018b). An improved permeability evolution model and its application in fractured sorbing media. J Nat Gas Sci Eng, 56: 222–232

Wang X M, Wang X M, Pan Z J, Yin X B, Chai P C, Pan S D, Yang Q (2019). Abundance and distribution pattern of rare earth elements and yttrium in vitrain band of high-rank coal from the Qinshui Basin, northern China. Fuel, 248: 93–103

Wang G, Han D Y, Jiang C H, Zhang Z Y (2020a). Seepage characteristics of fracture and dead-end pore structure in coal at micro- and meso-scales. Fuel, 266: 117058

Wang M F, Wang J J, Tao S, Tang D Z, Wang C C, Yi J (2020b). Quantitative characterization of void and demineralization effect in coal based on dual-resolution X-ray computed tomography. Fuel, 267: 116836

Wang H, Yao Y B, Huang C C, Liu D M, Cai Y D (2021). Fault development characteristics and their effects on current gas content and productivity of No.3 coal seam in the Zhengzhuang Field, southern Qinshui Basin, north China. Energ Fuels, 35(3): 2268–2281

Yuan C, Chareyre B, Darve F (2016). Pore-scale simulations of drainage in granular materials: finite size effects and the representative elementary volume. Adv Water Resour, 95: 109–124

Zhang Y X, Yuan Q, Huang D, Kong S F, Zhang J, Wang X F, Lu C Y, Shi Z B, Zhang X Y, Sun Y L, Wang Z F, Shao L Y, Zhu J H, Li W J (2018). Direct observations of fine primary particles from residential coal burning: insights into their morphology, composition, and hygroscopicity. J Geophys Res Atmos, 123(22): 12964–12979

Zhang K, Sang S X, Zhou X Z, Liu C J, Ma M Y, Niu Q H (2021). Influence of supercritical CO_2-H_2O-caprock interactions on the sealing capability of deep coal seam caprocks related to CO_2 geological storage: a case study of the silty mudstone caprock of coal seam No. 3 in the Qinshui Basin, China. Int J Greenh Gas Control, 106: 103282

Zheng S J, Yao Y B, Elsworth D, Liu D M, Cai Y D (2020). Dynamic fluid interactions during CO_2-ECBM and CO_2 sequestration in coal seams. Part 2: CO_2-H_2O wettability. Fuel, 279: 118560

Zhu Q Z, Wang X L, Zuo Y Q, Pan J N, Ju Y W, Su X F, Yu K (2020). Numerical simulation of matrix swelling and its effects on fracture structure and permeability for a high-rank coal based on X-ray micro-CT image processing techniques. Energ Fuels, 34(9): 10801–10809